AGU PUBLICATIONS

JGR

Journal of Geophysical Research: Atmospheres

RESEARCH ARTICLE

10.1002/2013JD020482

Special Section:
Suomi NPP Calibration and Validation Scientific Results

This article is a companion to *Seftor et al.* [2014] doi:10.1002/2013JD020472.

Key Points:
- The OMPS Limb instrument is performing nominally
- Sensor stray light is low
- Instrument pointing errors are greater than expected

Correspondence to:
G. Jaross,
glen.jaross@nasa.gov

Citation:
Jaross, G., P. K. Bhartia, G. Chen, M. Kowitt, M. Haken, Z. Chen, P. Xu, J. Warner, and T. Kelly (2014), OMPS Limb Profiler instrument performance assessment, *J. Geophys. Res. Atmos.*, *119*, 4399–4412, doi:10.1002/2013JD020482.

Received 30 JUN 2013
Accepted 18 DEC 2013
Accepted article online 22 DEC 2013
Published online 11 APR 2014

OMPS Limb Profiler instrument performance assessment

Glen Jaross[1], Pawan K. Bhartia[1], Grace Chen[2], Mark Kowitt[2], Michael Haken[2], Zhong Chen[2], Philippe Xu[3], Jeremy Warner[2], and Thomas Kelly[2]

[1]NASA Goddard Space Flight Center, Greenbelt, Maryland, USA, [2]Science Systems and Applications, Inc., Lanham, Maryland, USA, [3]Science Applications International Corp., Beltsville, Maryland, USA

Abstract Following the successful launch of the Ozone Mapping and Profiler Suite (OMPS) aboard the Suomi National Polar-orbiting Partnership (SNPP) spacecraft, the NASA OMPS Limb team began an evaluation of instrument and data product performance. The focus of this paper is the instrument performance in relation to the original design criteria. Performance that is closer to expectations increases the likelihood that limb scatter measurements by SNPP OMPS and successor instruments can form the basis for accurate long-term monitoring of ozone vertical profiles. The team finds that the Limb instrument operates mostly as designed and basic performance meets or exceeds the original design criteria. Internally scattered stray light and sensor pointing knowledge are two design challenges with the potential to seriously degrade performance. A thorough prelaunch characterization of stray light supports software corrections that are accurate to within 1% in radiances up to 60 km for the wavelengths used in deriving ozone. Residual stray light errors at 1000 nm, which is useful in retrievals of stratospheric aerosols, currently exceed 10%. Height registration errors in the range of 1 km to 2 km have been observed that cannot be fully explained by known error sources. An unexpected thermal sensitivity of the sensor also causes wavelengths and pointing to shift each orbit in the northern hemisphere. Spectral shifts of as much as 0.5 nm in the ultraviolet and 5 nm in the visible, and up to 0.3 km shifts in registered height, must be corrected in ground processing.

1. Introduction and Background

The first significant attempt at sensing radiances from the Earth limb was the LIMS instrument flown on NASA's Nimbus 7 spacecraft in 1978. This instrument and many of its successors were designed to measure the thermal emissions of atmospheric constituents, and thereby retrieve their concentrations. It was not until 1996, with the Shuttle Ozone Limb Scattering Experiment (SOLSE) and the Limb Ozone Retrieval Experiment (LORE) [*McPeters et al.*, 2000], that the more challenging retrieval from limb scattered radiances was attempted successfully. Subsequent missions designed for limb scattering measurement include the Optical Spectrograph and Infrared Imaging System (OSIRIS) [*Llewellyn et al.*, 2004] launched on the ODIN satellite in 2001 and the Scanning Imaging Absorption Spectrometer for Atmospheric Cartography (SCIAMACHY) [*Bovensmann et al.*, 1999] launched on the ENVISAT satellite in 2002.

The Ozone Mapping and Profiler Suite (OMPS) was proposed by Ball Aerospace and Technology Corporation as the ozone measurement component of the National Polar-Orbiting Environmental Satellite System (NPOESS) in 1998. Following the success of SOLSE and LORE, a limb scatter sensor was chosen to satisfy the ozone vertical profile requirements of the original NPOESS program. The first satellite of the successor program, the Suomi National Polar-orbiting Partnership (SNPP) spacecraft, was launched on 28 October 2011. The OMPS Limb Profiler collected its first Earth limb data in January 2012.

Limb sensors image the Earth atmosphere by viewing it "on edge" from space. The closest approach of the sensor line of sight to the Earth surface is referred to as the tangent point; this is the point where the sensor line of sight intersects an Earth radius vector at a right angle and where the retrieval algorithms calculate constituent gas or aerosol amounts. The altitude of this point above the Earth geoid is referred to as the tangent height. In limb scatter measurements sunlight scatters off particles or molecules and into the line of sight. Not only do photons scatter all along the 1000 km portion that passes through the atmosphere, but they can be absorbed anywhere as well. Furthermore, a photon may have already scattered at least once prior to the final scatter that sends it toward the sensor. The task of simulating reflected Earth radiances at the top of the atmosphere over a range of wavelengths and a variety of

©2013. American Geophysical Union. All Rights Reserved.

Table 1. Instrument Design Parameters

Parameter	Value
Wavelength range	290 – 1000 nm
Bandwidth (FWHM)	1 – 40 nm (2 pixels / FWHM)
Vertical sampling / instantaneous resolution	1 km / 1.5 km
Ozone vertical coverage	tropopause – 60 km
Ozone accuracy	
below 15 km	20% or 0.1 ppmv
above 15 km	10% or 0.1 ppmv
Ozone precision	
below 15 km	10% or 0.1 ppmv
15 – 50 km	3% or 0.05 ppmv
50 – 60 km	10% or 0.1 ppmv
Long-term relative ozone accuracy	2% / 7 years

viewing conditions falls to the radiative transfer model [*Herman et al.*, 1995]. In an iterative procedure within the retrieval code [*Flittner et al.*, 2000; *von Savigny et al.*, 2003; *Degenstein et al.*, 2009; *Rault and Loughman*, 2013], the atmospheric constituent (ozone, in this case) amounts are varied as inputs to the model until an optimum match with the measured radiances is achieved.

2. Instrumentation

The optical and electrical design of the OMPS Limb instrument has been previously described by *Dittman et al.* [2002] and *Leitch et al.* [2003]. The Limb instrument for OMPS was designed to meet its sole requirement of measuring the vertical profile of atmospheric ozone concentration between the tropopause and 60 km. These accuracy and precision requirements are broadly described in *Flynn et al.* [2007] and shown in Table 1. Though previous instruments using the limb scatter technique have successfully measured stratospheric aerosols [*Taha et al.*, 2011; *Bourassa et al.*, 2012], NO_2 [*Sioris et al.*, 2003], polar mesospheric clouds [*von Savigny and Burrows*, 2007], and other trace gas species, these measurements were not required and did not factor into the OMPS design. As a consequence, several simplifying aspects were employed. One important difference between OMPS and other limb scatter sensors is the use of a prism disperser rather than a diffraction grating. The prism, which has a highly nonlinear dispersion, was selected because it allows for reduced detector size and is suited for ozone measurements. The resulting spectral resolution, 1 nm in the ultraviolet and 10 nm in the visible, is comparable to the spectral structure of the Hartley, Huggins, and Chappuis ozone absorption bands. This means the instrument is ill suited to the kind of spectroscopy needed to retrieve other trace gas species. Measurement of stratospheric aerosols, which requires only broadband radiometry, is within the capability of this design. For the purposes of discussion, the following OMPS wavelength ranges are defined, UV: 290 to 370 nm, VIS: 370 to 750 nm, IR: 750 to 1000 nm.

Another important distinction of the OMPS instrument design is that it collects Earth limb radiance simultaneously from all altitudes. Most limb scatter sensors scan vertically through atmosphere, obtaining signals sequentially at different tangent heights. An exception is the infrared imager in the OSIRIS instrument [*Llewellyn et al.*, 2004], which views approximately 100 km of the Earth limb in each of its three channels. Because of the OMPS operational status within the United States' polar-orbiting program, a scanning mirror mechanism whose failure would result in complete loss of the data product was avoided. The successful use of a charge coupled device (CCD) detector on SOLSE to simultaneously capture the spectrally dispersed photons and their vertical distribution led to a similar design for OMPS Limb. The two-dimensional detector design eliminates the slight change in geographic location that results as an instrument scans vertically while the spacecraft moves. But it also introduces new challenges related to internally scattered stray light, reduced flexibility in managing the large dynamic range of signal inputs, and spatial variability in the radiometric response.

2.1. General Design

The Ozone Mapping and Profiler Suite consists of three main components: the Nadir instrument, the Limb instrument, and the Main Electronics Box (MEB). *Seftor et al.* [2013] provide a description of the Nadir instrument and its performance. The three OMPS components are mounted together on a baseplate that sits at the aft end of the SNPP spacecraft. The spacecraft flies in a nominal 1330 local time ascending, sun-synchronous orbit. Because the Limb instrument has a fixed field of view, the optical axis of its telescope tilts downward relative to the baseplate by 27.3°. The limb view tangent points pass each geographic location approximately 7 min after they are viewed by the Nadir instrument. A long, vertical slit provides a 1.85° field of regard that views the Earth limb from the side. There are, in fact, three slits separated horizontally by 4.25°, which translates to 250 km separation of the tangent points at the Earth surface. The vertical fields of view at the tangent points extend 105 km, each sampled by 105 spatial pixels at each wavelength. The extent in excess of the tropopause to 60 km requirement was needed to account for orbital and seasonal variations in

©2013. American Geophysical Union. All Rights Reserved.

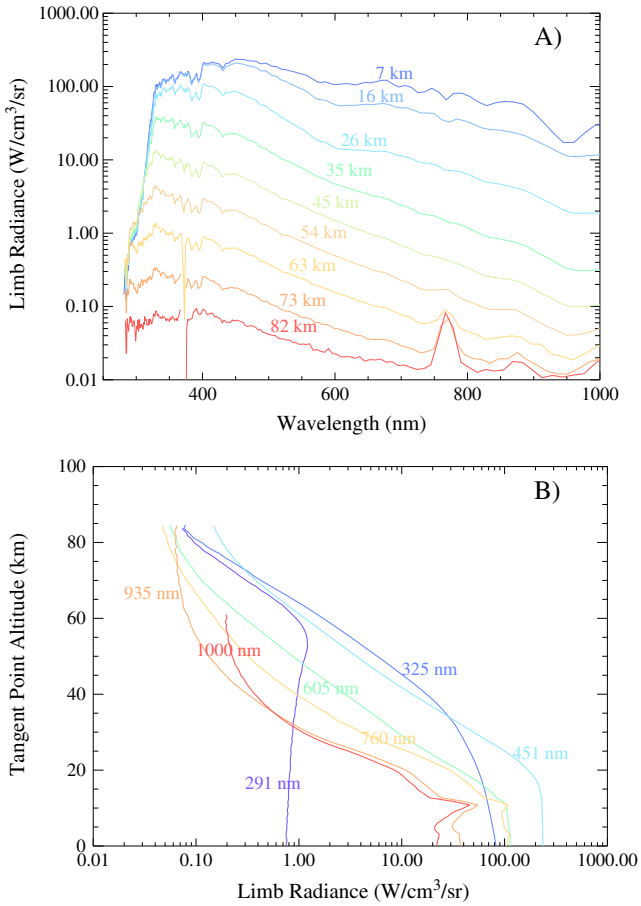

Figure 1. An example of Earth limb radiances measured in the OMPS center slit, small aperture on 13 August 2012 at 45° north latitude. The measured spectra at a sample of tangent heights are shown in Figure 1a. Radiances profiles from the same measured image are shown in Figure 1b for several wavelengths. The convergence of the high altitude lines in Figure 1a and the upward curve of the profiles in Figure 1b is an indication of residual stray light errors. For a given altitude, these errors are worse for longer wavelengths.

SNPP spacecraft pointing and sensor mounting uncertainties. In orbit, the maximum tangent height ranges between 80 km and 100 km, depending on latitude.

Regardless of how the radiance data are normalized prior to retrieval, limb scatter measurements are not entirely self-calibrating. This is especially true of OMPS where detector pixels can drift independently. The Limb instrument was required to maintain 2% relative accuracy in ozone over 7 years, so some means was needed to maintain radiometric stability over the course of the mission. Like other backscatter ultraviolet (BUV) instruments, the Nadir and Limb instruments use diffusers in the field of view to measure solar flux. Long-term variation of the measured flux yields an estimate of the combined changes in sensor response and true solar irradiance. The Limb instrument's transmissive diffuser rotates in front of the telescope so that the entire optical path, with the exception of the diffuser itself, is used for both Earth and solar measurements. Following the approach of heritage instruments [*Jaross et al.*, 1995], a second, infrequently exposed, diffuser is used to monitor degradation of the primary diffuser.

Between the Earth's surface and 100 km limb scattered radiances vary by as much as 5 orders of magnitude within each orbit as a result of decreasing particle density (see Figure 1). This dynamic range poses unique challenges when the radiances are measured simultaneously rather than sequentially, as when scanned. The well depth of a CCD is no more than 7×10^5 electrons, so gain settings that allow the lowest altitudes to remain unsaturated provide insufficient signal at high altitudes. The OMPS electronics do not allow for variations in the gain or integration time across the CCD detector. The solution employed by OMPS is to collect interleaved images of the full atmosphere at two different integration times. These two integration times differ by a factor of 31. The sensor also increases dynamic range by collecting the full range of radiances

©2013. American Geophysical Union. All Rights Reserved.

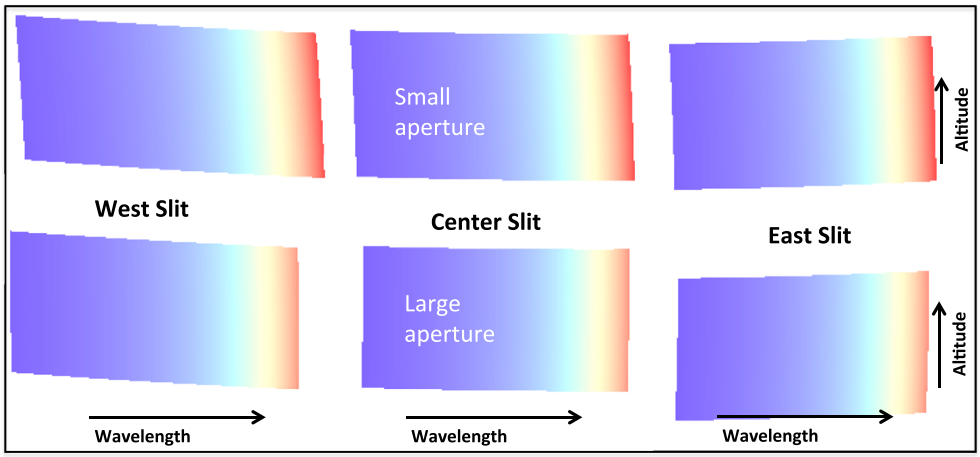

Figure 2. A schematic representation of the focal plane layout showing the six sets of atmospheric spectra (two apertures for each of three slits) obtained from OMPS. Each aperture's image has an approximate extent of 100 spatial pixels and 200 spectral pixels. The border indicates the physical extent of the detector. Colors representing the wavelength registration at the focal plane are not meant to be accurate, but do indicate the nonlinear dispersion of the spectrometer.

simultaneously through a large and a small aperture. The signals at the focal plane differ by a factor of 4.5 for the two aperture paths. Since there are three entrance slits, a total of six full atmospheric spectra are imaged at the focal plane. The focal plane layout is shown in Figure 2. The multiple integration times, multiple apertures, and CCD well capacity give the sensor a dynamic range capability of nearly 10^7. It remains for the ground processing algorithm to select the most sensitive, unsaturated signals and combine the multiple measurement sets into a single radiance profile. For the VIS and IR radiances, a maximum signal/noise ratio over the full altitude range is obtained by interleaving data from all four individual measurement sets. In the UV, only three are needed.

2.2. Operations and Data Processing

The OMPS MEB contains most of the suite electronics, including timing and clocking boards, the analog-digital converters, and the central processor unit (CPU). There is only one CPU controlling the single interface to the spacecraft, so the measurement times of the Nadir and Limb must be carefully synchronized and they share a common data rate cap. This cap is several orders of magnitude below the capability of OMPS to generate data. The necessary data reduction occurs within the MEB where pixel signals are sampled and combined. In the case of the Limb instrument, signals from fewer than 30% of the available pixels are sent to the ground. And those signals are accumulated over 18.5 s for each limb image, yielding 160 images below 88° solar zenith angle each orbit. The OMPS measurement timing and pixel sampling are fully configurable, so all numbers are subject to change as measurement techniques are optimized.

Pixel selection within OMPS is controlled by an uploaded sample table, so the first job of ground processing is correctly identifying each pixel represented in the data stream and assigning a tangent height and band center wavelength. The pixel counts themselves are corrected for detector bias and CCD readout smear. The thermal-induced dark signals, estimated from dedicated measurements during Earth night, are subtracted. Detector nonlinearity is corrected within the instrument rather than in ground processing. Stray light, estimated using the technique described in section 3.4, is also subtracted at the count level. Finally, the corrected counts are multiplied by pixel calibration coefficients to yield calibrated radiances.

Several steps are taken prior to reporting calibrated radiances. Depending on the sample table used, some fraction of pixel signals are collected using both long and short integration times. Only the longest, unsaturated measurement is used in subsequent processing. Optical distortions at the focal plane, seen in Figure 2, result in detector columns and rows that are not rectilinear in tangent height and wavelength. Since most retrieval algorithms rely upon a series of monochromatic radiance profiles, bilinear interpolation is employed [*Rault and Loughman*, 2013] to yield six sets of radiances on a spectral-spatial grid, one set for each aperture.

©2013. American Geophysical Union. All Rights Reserved.

Table 2. Instrument Performance Criteria

Parameter	Value
Radiance / Irradiance calibration ratio RMS uncertainty	
absolute	2%
relative, between wavelengths	0.5%
Wavelength Calibration RMS uncertainty	0.01 · FWHM (290 – 370 nm)
	0.03 · FWHM (370 – 1000 nm)
Linear polarization sensitivity	≤ 1%
Stray light (before correction)	≤ 8.5% at 62 km T.H., 290 nm
	≤ 3.1% at 45 km T.H., 500 – 675 nm
	≤ 45.7% at 45 km T.H., 1000 nm
Nonlinearity knowledge (zero input signal to full CCD well)	0.2%
Pixel-to-pixel response knowledge	0.2%
Pixel pointing knowledge (pitch, 3σ)	±0.035 deg. (approximately ±2 km tangent height)
Alignment change (per axis, 3σ)	0.08 deg. (ground to on-orbit)
	0.06 deg. (intraorbital)

Interpolation errors are primarily a result of sensor undersampling of the backscattered solar Fraunhofer spectrum. These errors can be as large as 5% but have a median of 0.7% between 290 and 365 nm.

Consolidation of large and small aperture radiances for each slit is possible at this stage because both are interpolated to the same spectral-spatial grid. There are several options for combining these measurement sets. When the instrument was designed, the belief was that maximizing detector signal without saturating would yield the best radiance profiles. In that case, the algorithm would naturally select between both long and short integration times and large and small apertures at different altitudes. In-flight data have revealed that radiance differences between large and small aperture measurements can differ systematically by several percent. This contrasts with detector noise that exceeds 0.5% only at tangent heights above 60 km. These systematic differences result from residual stray light errors in the small aperture radiances at high tangent heights, relative errors in tangent height between the two apertures, and radiance gridding errors. Statistically significant differences between large and small apertures can be observed at all altitudes and wavelengths. This is not the case when comparing long and short integration times for a given pixel. For this reason, radiance profiles at a specific wavelength are only reported from one aperture. In the UV, this is always the large aperture.

3. Calibration and Performance

As part of the Limb instrument system design, a set of performance criteria was developed whereby the instrument and ground processing algorithms could demonstrably meet the ozone profile requirements listed in Table 1. Criteria such as wavelength registration and radiometric calibration represented the state of the art of the technique, while stray light and height registration became targets in the design development. The most important performance criteria are listed in Table 2 and are discussed in more details below.

The required instrument performance always depends on the error sensitivity of the proposed retrieval. Ozone retrievals from OMPS [*Rault and Loughman*, 2013] follow the prescription of *Flittner et al*. [2000], utilizing altitude normalization and wavelength pairs and triplets. In altitude normalization, the radiance at one tangent height is divided by the radiance at a reference height, 65 km in the UV and 45 km in the VIS. Ozone profile retrievals in the UV and VIS are performed separately and merged in the final product. In the UV, the altitude normalized radiances at multiple ozone absorbing wavelengths are also divided by ozone insensitive normalized radiances at or near 350 nm. Normalized radiances at 600 nm are divided by the weighted average of a longer and a shorter ozone insensitive radiance. The resulting measurement vectors make the retrievals superbly insensitive to multiple sources of systematic error. Many test setup and source errors during laboratory calibrations cancel in the retrievals. However, the algorithm does not have reduced sensitivities to wavelength registration, tangent height, or additive errors.

3.1. Detector Performance

The CCD detectors for OMPS Limb operate at −45°C to minimize temperature-induced dark current and other noise sources caused by lattice impurities. Like those of the Nadir sensor, the Limb CCD is equipped with antiblooming drains to prevent photoelectrons in saturated pixel wells from bleeding into neighboring

©2013. American Geophysical Union. All Rights Reserved.

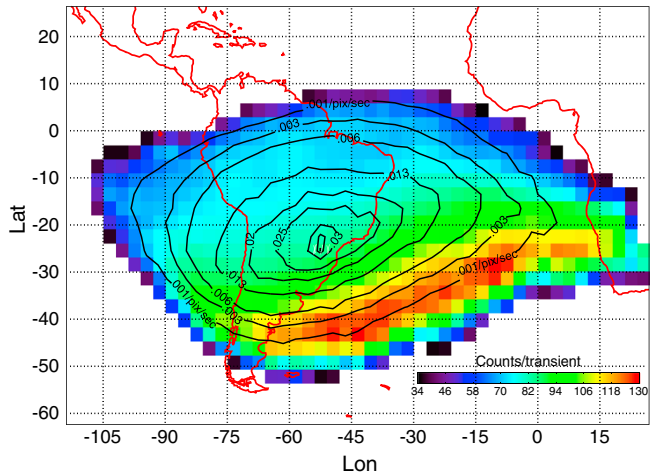

Figure 3. Transient observations in and around the South Atlantic Anomaly. Latitudes and longitudes indicate the satellite position, so tangent point latitudes where data are affected are 25° further south. Contours indicate the number of detected transients per pixel, per second. Colors indicate the mean signal level of the transients.

pixels. This is critical for the operation of this instrument because a very large number of low altitude pixels saturate at long integration times.

The most important characteristics of detector performance include dark current level and stability, response linearity, and sensitivity to transients. The first two characteristics are corrected accurately and introduce only minor errors in the reported radiances. Since the OMPS Nadir and Limb instruments carry nearly identical detectors, the description of dark currents and linearity in *Seftor et al.* [2013] for the OMPS Nadir detector provides interested readers with an accurate representation of Limb detector performance.

Energetic charged particles, particularly in the South Atlantic Anomaly (SAA), penetrate the CCD shielding and cause transients in pixel signals. Differences in detector orientation and pixel aggregation between the OMPS sensors means that the resulting radiance errors can be quite different. Affected pixels can be flagged in ground software and eliminated from subsequent atmospheric retrievals. As of this writing, the flagging algorithm does not perform well enough to report its performance. Data collected with the main sensor door closed were used to assess the energy and geographic distribution of the Limb detector transients. Thresholds for transient identification can be set very low when thermal electrons are the only other source of signal in pixel wells. Figure 3 displays both the rate of detected transients and their relative energy deposited in the CCD. As expected, the number of transients coincides with the known outlines of the SAA. At the center of the SAA, there is a 48% probability of each pixel encountering a transient during a Limb 12.5 s long exposure image. This probability decreases by a factor of 21 when short exposures are used, which typically occurs in the troposphere and lower stratosphere.

The maximum energy of transients is not centered on the SAA but instead peaks somewhat to the south and east. This observation is the same for both the Nadir detectors. The geographic separation is consistent with observations by other spacecraft [*Hajdas et al.*, 2003] that protons tend to be trapped to the north of electrons within the anomaly. This implies that OMPS signals are predominantly affected by protons and that electrons generate fewer but larger transients.

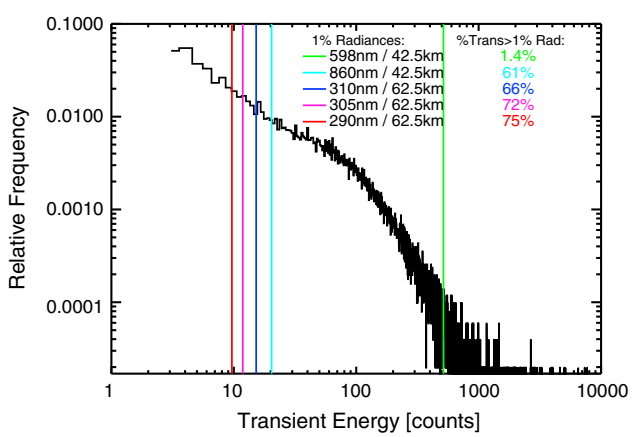

Figure 4. The energy distribution of transients at the center of the SAA, expressed in sensor counts, is shown along with lines indicating 1% of the energy deposited by backscattered photons at a similar latitude. The probability that a transient exceeds the 1% level is noted in the figure.

The effect of transients on measured Limb sensor radiances is complicated. Because the sensor looks aft along the spacecraft track, radiance profiles just off the Atlantic coast of Antarctica are most affected. Figure 4, which shows the transient energy distribution in the SAA center, demonstrates a high probability for low energy transients with high energy transients being relatively rare. The likelihood that a transient will exceed a 1% radiance error is

©2013. American Geophysical Union. All Rights Reserved.

shown in the same figure for several important wavelengths. When a pixel at the reference altitude is struck by a charged particle, as many as three fourths of those hits will cause greater than 1% radiance error.

3.2. Wavelength Calibration

Knowledge of pixel band center wavelengths and band-pass responses is needed to correctly compute ozone absorption cross sections. Between 290 and 320 nm, the absorption decreases dramatically, 10% to 20% per nanometer, so a small error in band center can significantly affect retrieved ozone concentrations. The broad spectral dependence of the ozone absorption in the VIS leads to a much smaller sensitivity. The primary cause of band center error in OMPS is changes in alignment of the spectrometer optics, which means the error is in the same direction and nearly the same at all wavelengths when measured as a fraction of a spectral pixel. Because the Limb sensor dispersion is approximately 10 times larger at 600 nm than at 300 nm, the ozone retrieval sensitivity to alignment shifts is similar in UV and VIS.

Like other hyperspectral instruments measuring in the ultraviolet and shortwave visible spectrum, OMPS depends on the well-characterized Fraunhofer structure in the solar spectrum to establish and maintain its spectral registration. Nonlinear regression with basic parameters of wavelength shift and dispersion, *dλ/dpixel*, is the typical approach and is described in more detail in the *Seftor et al*. [2013]. In the case of OMPS Limb, a reference spectrum composed of solar measurements from satellite, balloon, and ground [*Dobber et al*., 2008; *Chance and Kurucz*, 2010] is convolved with the OMPS pixel band passes. Regressions against the reference in three independent fit windows between 290 nm and 435 nm are combined and extrapolated to longer wavelengths. The few deep Fraunhofer lines longer than 500 nm are measured at poor resolution, rendering them useless in the dispersion regression. The prism dispersion must be known accurately to fit the Fraunhofer lines and to extrapolate the wavelength registration to the near infrared. With diffraction gratings, the extrapolation errors are relatively small because of their nearly constant dispersion. In fused silica, the dispersion changes most rapidly in the IR. Fortunately, the refractive properties of the fused silica used for the OMPS prism are known quite well.

Sellmeier's equation [*Jenkins and White*, 1957] describes the refractive index of many materials that exhibit anomalous dispersion.

$$n^2(\lambda) = 1 - \lambda^2 \sum_{k=1}^{3} \frac{B_k}{\lambda^2 - \lambda_k^2} \tag{1}$$

In this equation, n is the wavelength-dependent index of refraction of the OMPS prism. B_k and λ_k are known constants for the sensor prism material, Dynasil 1103. Rather than characterizing dispersion as the change in wavelength per pixel, the change in index of refraction squared per pixel is characterized. The advantage of this is the relationship between pixel number and n^2 is nearly linear. Thus, the wavelength registration problem reduces to one quite similar to that of grating spectrometers. In the regression, the optimal zero and first-order coefficients relating n^2 to pixel number are derived relative to the reference solar spectrum. The value of n^2 thus estimated for each pixel is uniquely converted back to a band center wavelength via equation (1). A preliminary linear regression using a second-order polynomial in wavelength is used to scale the measured solar flux to achieve a better match with the reference flux and thus improve the basis for the spectral regression. An independent wavelength registration is obtained for each of the approximately 100 solar spectra measured in each of the six OMPS apertures.

The quality of the wavelength registration is evaluated by examining regression residuals, such as those shown in Figure 5. The difference plots, shown in Figures 5b and 5c, are the equivalent of regression residuals except they also include the radiometric differences previously removed by the second-order polynomial. The ±1% residual structure for wavelengths between 300 nm and 360 nm is typical of a characterization within 1/100 of a spectral pixel. The n^2 extrapolation to wavelengths shorter than 290 nm appears to be less accurate. The residual structure is often shared between the spectra measured at different spatial locations on the detector, suggesting that they are caused by systematic sources of error such as radiometric calibration either of OMPS or in the reference spectrum.

A time series of the sensor wavelength registration, shown in Figure 6, indicates a significant seasonal cycle that is probably related to the solar flux incident on OMPS and resulting thermal changes. Sensor temperature is expected to affect both optics alignment and the prism index of refraction. The measured changes in prism

©2013. American Geophysical Union. All Rights Reserved.

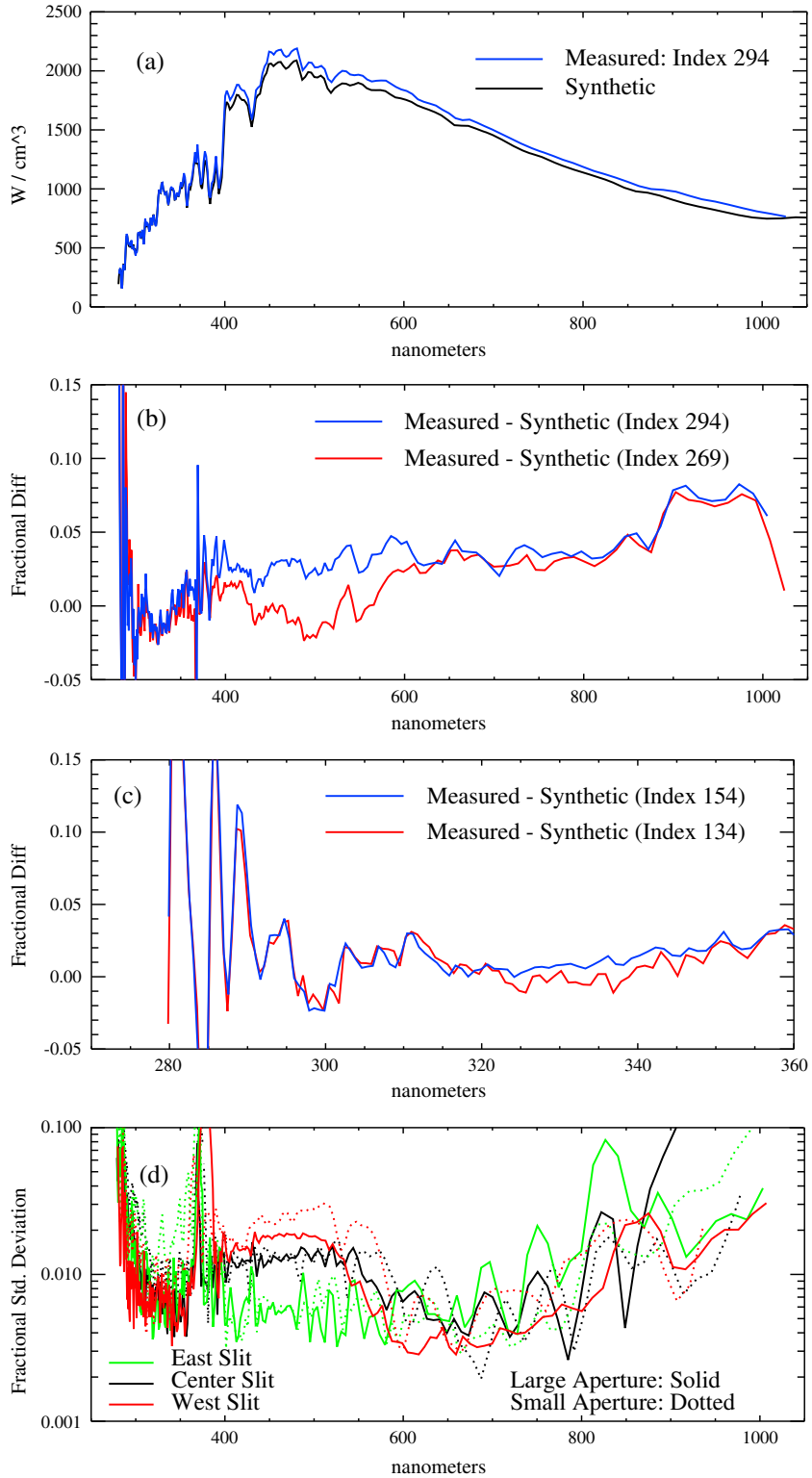

Figure 5. A comparison between measured and synthetic solar irradiance shown for selected detector spatial indexes in the west slit. Each spatial index is a distinct tangent height when measuring Earth radiance but should yield identical solar measurements. (a) Overall solar irradiance. (b) Fractional difference between measured and synthetic spectra at two spatial locations. (c) A magnified view of the UV spectra. (d) Standard deviation of the spatial variation at each wavelength for each of the six apertures.

©2013. American Geophysical Union. All Rights Reserved.

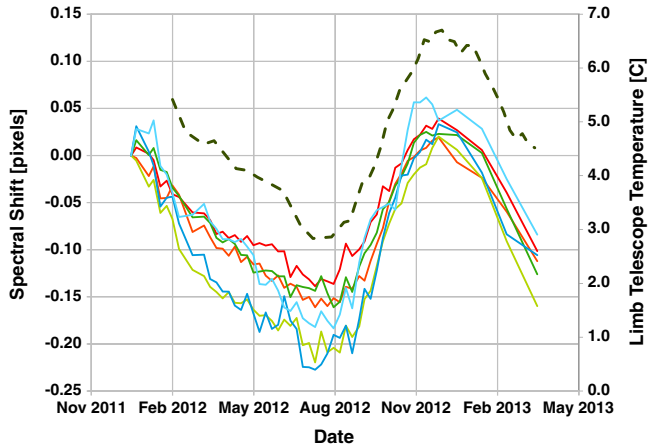

Figure 6. The seasonal cycle of band center shifts derived from regression of weekly solar measurements shown as a colored line for each of the six apertures. The shift is expressed in spectral pixels. A 1 pixel shift is approximately equal to 1 nm at 300 nm and 10 nm at 600 nm. The correlation with instrument temperature, shown as the dashed line, suggests a thermal-induced shift of spectrometer optical alignment.

temperature are too small to change its refraction significantly and the time series of n^2 regression coefficients confirms that the changes are almost entirely in the zero order, so the shifts are likely mechanical in nature.

3.3. Radiometric Accuracy

The insensitivity of retrieved ozone to Earth radiance errors, described in the introduction to section 3, would suggest there is little need for a well-calibrated instrument. While it is true that the ratios used by the retrieval cause many common radiometric errors to cancel, errors that depend on the vertical dimension do not. This is especially true in the VIS retrievals where a single absorbing wavelength is used over a large tangent height range. A 1% change in 600 nm radiance at 10 km results in a 2% change in retrieved ozone concentration there. A solar measurement capability was introduced on OMPS Limb to minimize altitude-dependent errors and related long-term calibration changes. Since the same detector pixels are used for measurements of both Earth radiance, *L*, and solar irradiance, *E*, many pixel response characterization errors will cancel in a *L/E* ratio. Pixel-to-pixel response errors contribute to altitude-dependent retrieval errors, so use of this ratio, also known as TOA reflectance, should improve retrievals. Use of reflectance also reduces the undersampling error described in section 2.2. The OMPS ozone retrieval algorithm does not currently use TOA reflectance, so an evaluation of solar irradiance can inform regarding the radiometric accuracy of radiance measurements used in retrievals.

The solar irradiance comparisons at two tangent heights, 20 km to 25 km apart, are shown in Figures 5b and 5c. These examples suggest height-dependent calibration errors are relatively small in the UV and IR, and larger in VIS. Figure 5d, which shows the solar irradiance standard deviation of approximately 100 spatial locations at each wavelength, provides an estimate of uncorrelated errors over the full tangent height range. With the exception of the IR wavelengths, relative errors are typically 1%. The increased variance in the IR that curiously occurs in wavelength bands may be caused by the CCD etalon effect, a result of the detector silicon becoming increasingly transparent at these wavelengths.

3.4. Stray Light Correction

Spectral-spatial detectors such as on OMPS are more susceptible to internally scattered stray light because photons from bright parts of a scene can scatter both spectrally and spatially into weaker signal regions. In the case of the Limb instrument, 330 to 370 nm photons from low altitudes are the dominant source of scattered light affecting high altitude signals shorter than 310 nm. Furthermore, with multiple images on a single detector, a significant portion of the stray light is interimage. Photons from the IR portion of one slit can easily scatter into the UV portion of its neighboring slit, and vice versa. Stray light in the small apertures is greater than in the large apertures because of interimage scattering. Back-reflections from the window covering the CCD also generate ghosts, but these do not contribute a significant level of stray light in the useful portions of the OMPS measured spectra.

The OMPS Limb approach to dealing with stray light is twofold: optical filtering and signal correction during ground processing. A filter to block visible wavelength photons is applied to the focal plane window for those portions of the detector that collect light shorter than 370 nm. The physical edge of the filter is matched to its cutoff wavelength so that visible light incident on the VIS portions of the detector is unaffected. This alone significantly reduces stray light in the high altitude UV wavelengths. Those data are used for ozone retrievals at altitudes above approximately 35 km.

©2013. American Geophysical Union. All Rights Reserved.

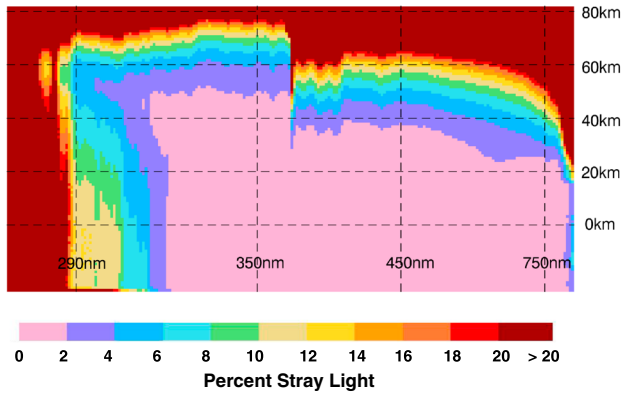

Figure 7. Calculated stray light percentages (7 February 2012), shown as a function of spectral and spatial pixel number, are based on the measured limb signal and the OMPS stray light model. Stray light percentages vary little with viewing conditions or season. The step near 370 nm corresponds to the edge of the detector window filter.

Stray light point spread functions (PSFs) were also extensively measured during sensor laboratory testing. During these tests, a tunable laser was used to create a series of spectral-spatial point sources. The full detector response to each point source, its PSF, was measured down a level of 10^{-9} times the source signal. A four-dimensional stray light Jacobian, in detector signal $C(i,j)$ and incident radiance $L(i,j)$, was constructed by interpolating these measured PSFs to intermediate source wavelengths and altitudes, then evaluating the function at each target pixel $(i_t,j_t)_{stray}$ when it is centered at pixel $(i_s,j_s)_{source}$. This Jacobian, when applied to the signals measured in orbit, is the basis for estimating the stray light signal $S(i_t,j_t)$ present in measured Earth limb signals.

$$S(i_t,j_t) = \sum_{i_s}\sum_{j_s} \frac{\partial C(i_t,j_t)_{stray}}{\partial L(i_s,j_s)_{source}} . L(i_s,j_s) \tag{2}$$

The stray light signal at a target pixel (i_t,j_t) is derived from the sum over all source radiances $L(i_s,j_s)$ contributing to that pixel. This process requires a second iteration to reduce residual errors below 1%. One complication with this approach is it requires an ensemble of radiance measurements $L(i,j)$ at all contributing wavelengths and spatial locations to prevent an underestimation of stray light. Fortunately, there are no significant stray light sources outside the spectral and spatial range measured by OMPS, and radiances missing due to the sparse sampling of the detector can be adequately estimated via interpolation.

An example of the stray light content of an Earth scene estimated using equation (2) is shown in Figure 7 for the center slit, large aperture image. Stray light percentages in other slits and apertures are qualitatively similar but differ due to interimage scattering. Values are provided for all slits in Table 3. As Figure 7 confirms, stray light is primarily a high altitude problem with levels in the UV less than 10% at altitudes below 60 km. Stray light percentages are greatest in the IR because the low Rayleigh cross sections there lead to the largest vertical signal gradients. A comparison between the design stray light allocations in Table 2 and the observed stray light in Table 3 suggests the sensor performs slightly worse than predicted. What ultimately matters for atmospheric retrievals is how well the corrections based on equation (2) work.

An estimate of the efficacy of the stray light corrections is obtained by observing dark areas of the detector. The six regions shown in Figure 2 are the only areas of the detector that receive direct photons. Any photons collected outside these regions were a result of internal scattering. The stray light estimation approach described above works equally well in these nonoptical regions and should directly predict the entire signal measured there. Scattered light varies only slowly across the detector so it is reasonable to assume that any differences between modeled and measured signal levels remain the same just inside and just outside the

Table 3. Stray Light (percent of signal) at 65 km[a]

	290 nm	302 nm	310 nm	320 nm	353 nm	500 nm	602 nm	750 nm
Before	9.4	10.4	8.3	7.0	5.1	18.3	23.8	34.2
Correction	10.8	11.3	8.9	7.5	5.8	20.3	26.6	36.7
	13.1	15.7	12.1	11.6	10.7	34.2	45.1	49.9
After	–	0.3	0.3	0.2	0.3	1.6	2.3	4.0
Correction	1.3	1.0	0.6	0.5	0.8	2.0	3.0	−5.1
	1.5	1.1	0.9	0.7	0.6	4.0	5.6	6.6

[a]The three entries are for the east, center, and west slit, large apertures.

©2013. American Geophysical Union. All Rights Reserved.

Table 4. Stray Light (Percent of Signal) in the Infrared[a]

	10 km	15 km	20 km	25 km	30 km	35 km	40 km	45 km
900 nm	2.6	4.5	6.3	10.7	18.6	29.7	47.2	75.7
before	2.8	4.6	6.1	9.5	17.0	31.4	47.1	61.4
correction	3.4	4.3	7.1	12.8	24.1	35.6	54.2	72.8
900 nm	−0.1	−0.1	−0.2	−0.5	−0.4	−0.5	−0.5	−0.6
after	2.5	1.8	2.9	2.1	1.9	2.9	6.4	10.8
correction	2.6	1.9	3.0	3.1	4.4	6.6	9.2	13.4
1000 nm	10.8	24.2	37.1	73.3	102.0	194.4	379.8	609.7
before	8.4	19.9	19.8	40.6	84.7	171.1	193.7	211.1
correction	13.4	21.0	27.8	57.5	115.5	134.6	118.1	244.9
1000 nm	−0.2	−0.5	−0.9	−2.2	−1.9	−2.0	−2.2	−2.9
after	15.4	14.9	14.8	13.9	15.1	27.0	45.1	69.3
correction	17.3	17.0	18.5	21.0	31.4	41.8	62.5	96.5

[a]The three entries are for the east, center, and west slit, small apertures.

optical region. The estimated stray light errors after correction, shown in Table 3, are computed by converting this residual stray light signal into a percent of the total signal. This estimation method, which is only accurate near the image edges, predicts that UV wavelengths are generally corrected to within 1% at 65 km, the retrieval algorithm's normalization height. The residual stray light at lower tangent heights is likely less, so 1% is the maximum UV error passed to the retrieval.

In the VIS and IR regions, the correction at 65 km is poorer than 1%, but these wavelengths are used only at lower altitudes where stray light levels before correction are already small. Based on the results in Table 3, the efficacy of most corrections is approximately 10:1, meaning a 1% residual error for every 10% of correction. The laboratory stray light characterization was poorer in the IR, and that is reflected in the validation results shown in Table 4. Multiple internal reflections within the CCD are a form of stray light unique to the IR that is difficult to characterize during laboratory testing.

3.5. Tangent Height Registration

Knowledge of instrument pointing in the pitch direction is needed to accurately calculate each pixel's tangent height. A 0.016° pitch error translates to approximately 1 km tangent height error, which in the lower stratosphere can result in as much as 30% error in ozone number density during Antarctic ozone hole conditions. For OMPS, this pointing knowledge is derived from a combination of the spacecraft ephemeris, spacecraft attitude, sensor mounting information, and pixel pointing characterization. The alignment tolerances provided in Table 2 predict pointing knowledge to within the equivalent of 2.2 km (1σ) at the tangent point. An initial evaluation of the reported Limb sensor tangent height suggests that errors are comparable to this number.

Limb scattering tangent heights are often verified [*von Savigny et al.*, 2005] by comparing measured radiances with model predictions based on climatological or correlative measurements of temperature, pressure, and ozone. One such technique [*Janz et al.*, 1996] utilizes radiances near 350 nm, which are not absorbed by ozone. An accurate prediction of these radiances requires knowledge of atmospheric pressure and underlying scene reflectivity. The dependence on reflectivity can be largely removed by considering the differential radiances at two altitudes, but the tangent heights thus derived still vary with the cloud distribution of the underlying scene. The effect of this scene heterogeneity on TOA radiances is difficult to model accurately. Radiances at 350 nm are also sensitive to the treatment in the radiative transfer model of multiple scattering and the assumed aerosol extinction. The tangent height uncertainty of this technique has been estimated at 350 m [*Rault and Loughman*, 2013; *Taha et al.*, 2008]. By concentrating analysis at high latitudes, especially in the south polar region, problems related to surface effects and aerosols are largely eliminated. Under these conditions, a radiance analysis using nonabsorbed wavelengths yielded tangent height errors of 1.05, 1.35, and 1.98 km for the east, center, and west slits, respectively. The positive values mean that vertical profiles are registered too high in altitude.

When the wavelength is decreased to 310 nm or shorter, photons cease to penetrate to the cloud layer and are unaffected by them. To minimize uncertainties associated with ozone absorption and aerosols, these short UV radiances should only be used above 50 km to assess tangent height. Radiance gradients between 50 and 60 km tangent height are approximately10% per kilometer, so a 1% radiance uncertainty translates into only 100 m height uncertainty. Higher altitudes will increase the sensitivity to tangent height errors, but

©2013. American Geophysical Union. All Rights Reserved.

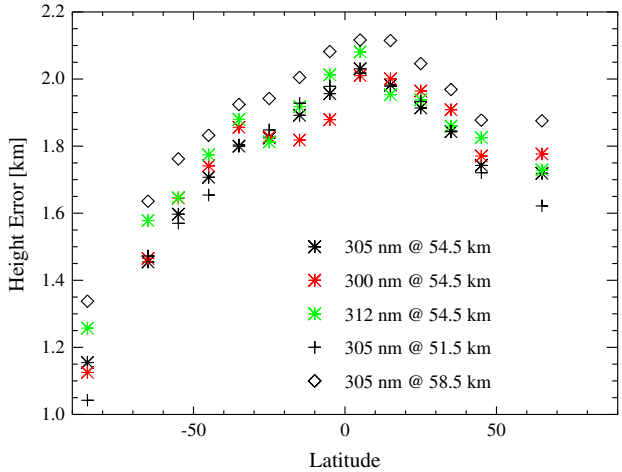

Figure 8. The tangent height error derived from the center slit difference between measured and calculated reflectances, averaged in 10° latitude zones for 19 October 2012. Coincident ozone, temperature, and pressure as a function of altitude from Aura/MLS were used in the calculations.

also the sensitivity to calibration errors. Stray light increases dramatically above 60 km, as does the uncertainty in atmospheric pressure, so this altitude represents a practical upper limit for this analysis.

For this evaluation, the Earth radiance to solar irradiance ratio, *L/E*, was modeled on the basis of atmospheric conditions measured on the same day by the Microwave Limb Sounder (MLS) on the Aura satellite. Ozone, geopotential height (GPH), and temperature as a function of pressure are provided in their version 3.3 release [*Livesey et al*., 2013]. The reflectance residuals, $\ln(L/E)_{\text{measured}} - \ln(L/E)_{\text{calculated}}$, are converted to tangent height differences using the calculated *L/E* gradient. Results averaged over 10° latitude bands for a full day are shown in Figure 8 for the center slit. The observed error of 1.0 to 1.4 km at 85° south latitude confirms the result from longer wavelengths, described above. The derived tangent height error in the east slit also ranges from 1.0 to 1.4 km, while in the west slit the range is 1.4 to 1.8 km. These errors, while large, are consistent with the intraorbital pointing uncertainty reported in Table 2. *Schwartz et al*. [2008] estimate a 300 m bias in the GPH reported by MLS at these altitudes, which would serve to decrease these apparent OMPS height errors. But a comparison with correlative data in the same publication also indicates that no bias exists.

The authors cannot easily explain the ~800 m shift in tangent height knowledge between the south pole and the equator. The 350 nm analysis described above yields a similar variation. Since MLS data were not used in that analysis, they are an unlikely source of the problem. The SNPP attitude determination system is also more precise than the observed 800 m, but the star trackers that are the primary source of SNPP pointing knowledge are located at the end of the spacecraft opposite to OMPS. It is possible that flexing of the spacecraft as a result of thermal gradients during each orbit can cause these latitude-dependent errors, though spacecraft models predict much smaller changes.

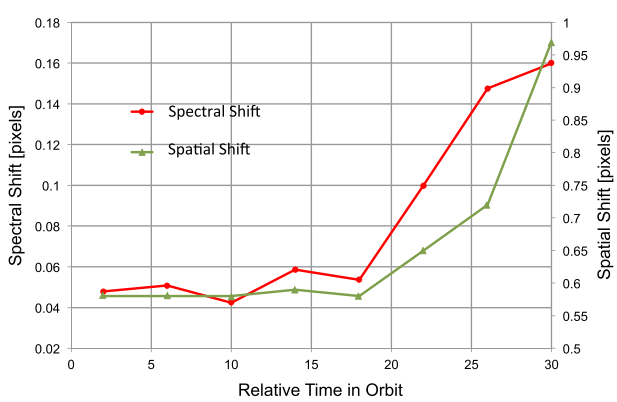

Figure 9. Spectral and spatial shifts of the east slit, large aperture image at the focal plane (relative to laboratory tests) as a function of time through each orbit. A time of 0 represents Earth day entry near the south pole, and a time of 30 represents Earth day exit near the north pole. A relative time of 18 corresponds to the approximate point in the orbit when the sun begins to illuminate and heat the instrument.

A contributing factor in the apparent sensor pointing errors was found by investigating the sensor's internal optical alignment. The vertical extent of each of the six images shown in Figure 2 is governed by the three slit lengths and the focusing optics. Any movement of the optics beyond these slits will translate the images on the focal plane. Since the bottom edge of each slit image is sharply defined in terms of detector signal, it

©2013. American Geophysical Union. All Rights Reserved.

is possible to track image motion in time. A comparison between image positions during laboratory tests and in flight indicates differences ranging from −0.3 to 0.9 pixels for the six images. A 1 pixel shift is equivalent to approximately 1 km error in tangent height. The authors conclude that internal shifts within the sensor, probably resulting from ground to on-orbit thermal changes, are responsible for half the vertical registration error observed at the south pole.

A further investigation of the image edge motion revealed that significant shifts also occur within each orbit. The shift observed in the large aperture, east slit data is shown in Figure 9. Similar shifts of varying magnitudes are observed in the other apertures. The shift, which occurs just over halfway through the day side of every orbit, makes the Limb sensor appear to point lower in the atmosphere by as much as 300 m. An analysis of sensor wavelength registration using the Earth radiance spectrum between 370 and 435 nm revealed a similar image shift in the spectral direction of the focal plane. The onset of both shifts coincides with the point in the orbit when the sun begins to illuminate the Limb instrument. Structural-thermal modeling of the instrument by the instrument manufacturer confirms that both shifts are a result of misalignment in the six secondary telescope mirrors. The model predicts that the instrument's entrance baffle, which is adjacent to these mirrors, experiences significant heating and expansion during each orbit, placing mechanical stress on the mirror mounts.

The assessment shown in Figure 8 is based on data that have been corrected for the intraorbital motion of the six images, though not for the ground-to-orbit shifts. There is no image motion in the southern hemisphere portion of each orbit, so that phenomenon does little to explain the 800 m variation seen in Figure 8.

4. Summary

The OMPS Limb instrument is performing quite well in flight and meeting all expectations for this stage of the mission. The full evaluation of performance goals is not yet complete, but important characteristics such as stray light and pointing have been investigated. There are no surprises in terms of sensor noise or calibration accuracy. Though not discussed above, the sensor remains radiometrically stable after 2 years in operation.

OMPS ozone retrievals use measured radiances normalized at a specific tangent height rather than the measured TOA reflectance. Based on laboratory calibration uncertainties, the latter should be more accurate. From an analysis of solar irradiance, the uncertainty in normalized radiance is within 1% for wavelengths used in ozone retrievals, so the benefit of using reflectance in retrievals will likely be minimal. However, this approach could become important as the instrument ages or for products where absolute signal levels are important.

With a few exceptions, sensor stray light is as expected, and ground corrections can eliminate most issues for the UV and VIS portions of the measured spectra. There remains a problem at wavelengths longer than 900 nm, where the magnitude of the stray light error increases dramatically with tangent height. This error will somewhat limit the ability to characterize aerosols in the middle and upper stratosphere. At 1000 nm, the residual stray light errors exceed 10% at all altitudes. Since this wavelength adds information related to aerosol particle size distributions, efforts will be made to improve the correction there.

Uncertain pointing remains a significant challenge for the Limb instrument. Tangent height errors have been evaluated several ways, and though results vary, there is general agreement that OMPS is registering limb radiances 1 to 2 km higher than it should be. The static component of this error is consistent with the uncertainty in instrument pointing and should be removed during data processing. Variations in the tangent height error within an orbit remain a mystery even though a known instrument thermal sensitivity causes some of the change. Without an independent verification of these orbital variations, the authors cannot recommend the application of a correction in ground processing.

Acknowledgments
The authors gratefully acknowledge the assistance of the Ozone Product Evaluation and Algorithm Test Element team at the NASA Goddard Space Flight Center in processing the data used in this evaluation. They also thank the OMPS team at Ball Aerospace Technology Corporation and the following persons for analysis and discussions that have furthered the understanding of these data: J. Larsen, R. Loughman, L. Moy, D. Rault, G. Taha, and S. Taylor.

References

Bourassa, A. E., L. A. Rieger, N. D. Lloyd, and D. A. Degenstein (2012), Odin-OSIRIS stratospheric aerosol data product and SAGE III intercomparison, *Atmos. Chem. Phys.*, *12*(1), 605–614, doi:10.5194/acp-12-605-2012.

Bovensmann, H., J. P. Burrows, M. Buchwitz, J. Frerick, S. Noël, V. V. Rozanov, K. V. Chance, and A. P. H. Goede (1999), SCIAMACHY: Mission objectives and measurement modes, *J. Atmos. Sci.*, *56*(2), 127–150.

Chance, K., and R. L. Kurucz (2010), An improved high-resolution solar reference spectrum for earth's atmosphere measurements in the ultraviolet, visible, and near infrared, *J. Quant. Spectrosc. Radiat. Transfer*, *111*, 1289–1295, doi:10.1016/j.jqsrt2010.01.036.

Degenstein, D. A., A. E. Bourassa, C. Z. Roth, and E. J. Llewellyn (2009), Limb scatter ozone retrieval from 10 to 60 km using a multiplicative algebraic reconstruction technique, *Atmos. Chem. Phys.*, *9*, 6521–6529.

©2013. American Geophysical Union. All Rights Reserved.

Dittman, M. G., J. Leitch, M. Chrisp, J. V. Rodriguez, A. Sparks, B. McComas, N. Zaun, D. Frazier, T. Dixon, R. Philbrick, and D. Wasinger (2002), Limb broad-band imaging spectrometer for the NPOESS Ozone Mapping and Profiler Suite (OMPS), Proc. SPIE 4814, Earth Observing Systems VII; pp. 120–130.

Dobber, M., R. Voors, R. Dirksen, Q. Kleipool, and P. Levelt (2008), The high-resolution solar reference spectrum between 250 and 550 nm and its application to measurements with the Ozone Monitoring Instrument, *Sol. Phys.*, *249*, 281–291, doi:10.1007/s11207-008-9187-7.

Flittner, D. E., P. K. Bhartia, and B. M. Herman (2000), O3 profiles retrieved from limb scatter measurements: Theory, *Geophys. Res. Lett.*, *27*, 2601–2604.

Flynn, L. E., C. J. Seftor, J. C. Larsen, and P. Xu (2007), The Ozone Mapping and Profiler Suite, in *Earth Science Satellite Remote Sensing*, edited by J. J. Qu et al., pp. 279–296, Springer, Berlin Heidelberg, doi:10.1007/978-3-540-37293-66.

Hajdas, W., C. Eggel, C. Wigger, D. Smith, H. Sanctuary, and A. Zehnder (2003), Spacecraft activation and south atlantic anomaly profiles measured with the RHESSI satellite, Proceedings of the 7th European Conference on Radiation and Its Effects on Components and Systems, RADECS 2003, 607–610.

Herman, B. M., T. R. Caudill, D. E. Flittner, K. J. Thome, and A. Ben-David (1995), Comparison of the Gauss-Seidel Spherical Polarized Radiative Transfer Code with other radiative transfer codes, *Appl. Opt.*, *34*(21), 4563–4572.

Janz, S. J., E. Hilsenrath, D. E. Flittner, and D. F. Heath (1996), Rayleigh scattering attitude sensor, Proc. SPIE 2831, Atmospheric Ultraviolet and Space Remote Sensing: Methods and Instrumentation, 146, doi:10.1117/12.257207.

Jaross, G., A. Krueger, R. P. Cebula, C. Seftor, U. Hartmann, R. Haring, and D. Burchfield (1995), Calibration and post-launch performance of the Meteor-3/TOMS instrument, *J. Geophys. Res.*, *100*(D2), 2985–2995, doi:10.1029/94JD02317.

Jenkins, F. A., and H. E. White (1957), Dispersion, in *Fundamentals of Optics*, 3rd ed., pp. 464–487, McGraw-Hill Book Company, Inc., New York.

Leitch, J. W., et al. (2003), Limb scatter ozone profiling sensor for the NPOESS Ozone Mapping and Profiler Suite (OMPS), Proc. SPIE 4891, Optical Remote Sensing of the Atmosphere and Clouds III; pp. 13-21.

Livesey, N. J., et al. (2013), Version 3.3 and 3.4 Level 2 data quality and description document. Technical report, Jet Propulsion Laboratory, D-33509, (http://mls.jpl.nasa.gov/data/v3_data_quality_document.pdf).

Llewellyn, E. J., et al. (2004), The OSIRIS instrument on the Odin spacecraft, *Can. J. Phys.*, *82*, 411–422.

McPeters, R. D., S. J. Janz, E. Hilsenrath, T. L. Brown, D. E. Flittner, and D. F. Heath (2000), The retrieval of O3 profiles from limb scatter measurements: Results from the Shuttle Ozone Limb Sounding Experiment, *Geophys. Res. Lett.*, *27*, 2597–2600.

Rault, D. F., and R. P. Loughman (2013), The OMPS Limb Profiler Environmental Data Record algorithm theoretical basis document and expected performance, *IEEE Trans. Geosci. Remote Sens.*, *51*(5-1), 2505–2527.

Schwartz, M. J., et al. (2008), Validation of the Aura Microwave Limb Sounder temperature and geopotential height measurements, *J. Geophys. Res*, *113*, D15S11, doi:10.1029/2007JD008783.

Seftor, C. J., G. Jaross, M. Kowitt, M. Haken, J. Li, and L. W. Flynn (2013), Post-launch performance of the Suomi NPP Ozone Mapping and Profiler Suite (OMPS) nadir sensors, *J. Geophys. Res. Atmos.*, *119*, 4413–4428, doi:10.1002/2013JD020472.

Sioris, C. E., et al. (2003), Stratospheric profiles of nitrogen dioxide observed by optical spectrograph and infrared imager system on the Odin satellite, *J. Geophys. Res.*, *108*(D7), 4215, doi:10.1029/2002JD002672.

Taha, G., G. Jaross, D. Fussen, F. Vanhellemont, E. Kyrölä, and R. D. McPeters (2008), Ozone profile retrieval from GOMOS limb scattering measurements, *J. Geophys. Res.*, *113*, D23307, doi:10.1029/2007JD009409.

Taha, G., D. F. Rault, R. P. Loughman, A. E. Bourassa, and C. von Savigny (2011), SCIAMACHY stratospheric aerosol extinction profile retrieval using the OMPS/LP algorithm, *Atmos. Meas. Tech.*, *4*, 547–556, doi:10.5194/amt-4-547-2011.

von Savigny, C., and J. P. Burrows (2007), Latitudinal variation of NLC particle radii derived from northern hemisphere SCIAMACHY/Envisat limb measurements, *Adv. Space Res.*, *40*(6), 765–771.

von Savigny, C., et al. (2003), Stratospheric ozone profiles retrieved from limb scattered sunlight spectra measured by the OSIRIS instrument on the Odin satellite, *Geophys. Res. Lett.*, *30*(14), 1755, doi:10.1029/2002GL0I6401.

von Savigny, C., J. W. Kaiser, H. Bovensmann, J. P. Burrows, I. S. McDermid, and T. Leblanc (2005), Spatial and temporal characterization of SCIAMACHY limb pointing errors during the first three years of the mission, *Atmos. Chem. Phys.*, *5*, 2593–2602, doi:10.5194/acp-5-2593-2005.

©2013. American Geophysical Union. All Rights Reserved.